

Self-Powered Triboelectric Micro Liquid/Gas Flow Sensor for Microfluidics

Jie Chen,^{†,§} Hengyu Guo,^{†,‡,§} Jiangeng Zheng,[†] Yingzhou Huang,[†] Guanlin Liu,[†] Chenguo Hu,^{*,†} and Zhong Lin Wang^{*,‡}

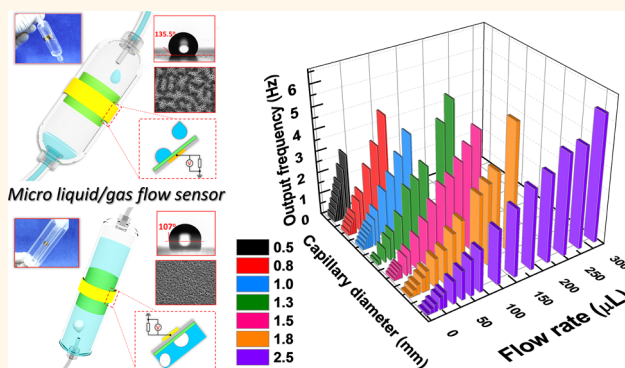
[†]Department of Applied Physics, Chongqing University, Chongqing 400044, China

[‡]School of Materials Science and Engineering, Georgia Institute of Technology, Atlanta, Georgia 30332-0245, United States

Supporting Information

ABSTRACT: Liquid and gas flow sensors are important components of the micro total analysis systems (μ TAS) for modern analytical sciences. In this paper, we proposed a self-powered triboelectric microfluidic sensor (TMS) by utilizing the signals produced from the droplet/bubble *via* the capillary and the triboelectrification effects on the liquid/solid interface for real-time liquid and gas flow detection. By alternating capillary with different diameters, the sensor's detecting range and sensitivity can be adjusted. Both the relationship between the droplet/bubble and capillary size, and the output signal of the sensor are systematically studied. By demonstrating the monitoring of the transfusion process for a patient and the gas flow produced from an injector, it shows that TMS has a great potential in building a self-powered micro total analysis system.

KEYWORDS: microfluidic sensor, triboelectric, self-powered system



Micro total analysis system (μ TAS) or lab on a chip (LOC) has been developed and investigated for more than 20 years, and now it has become a well-known analysis platform for biological, chemical, cellular, and nucleic acid analyses.^{1,2} As one of the analytical components, microfluidic sensors are widely used to build μ TAS in many industrial and commercial situations for monitoring and controlling mass-flow, flow velocity and flow volume.^{3–7} Conventional technologies are used to measure the fluidic and gas flow in μ TAS *via* the microparticle image velocimetry system⁸ and thermally actuated mechanism.⁹ However, the complex analysis equipment that include microscope, CCD camera, circulating system with high energy consumption largely limits their applications.¹⁰ Although, new devices based on acoustic,¹¹ thermal electric,¹² electromagnetic,¹³ and electrostatic effects¹⁴ have been developed and proposed for miniaturization and different applications, they are not quite suitable as sensors in μ TAS for practical situations due to their relative high cost and complicated working mechanisms.

In recent years, many kinds of triboelectric nanogenerators (TENG) based on the conjunction of triboelectrification and electrostatic effects have been developed and demonstrated for various energy related applications.^{15–24} Because of its simple structure and facile fabrication craft, TENG can be easily miniaturized to act as a mechanical sensor for detecting

vibration,^{25,26} wind speed,^{17,27} location,^{28,29} heart beating,³⁰ and so forth from various mechanical sources.³¹ Recently, on the basis of the triboelectrification and electrostatic induction between liquid and solid interface,^{32,33} a self-powered triboelectric nanosensor for microfluidic has been reported to detect the liquid flow rate. Through the fluidic channel design, it was used to directly characterize the chemistry synthesis.³⁴ Nevertheless, the liquid flow rate of the proposed nanosensor can be merely characterized once when the liquid flows through the detector, which cannot be used for real time monitoring and flow volume measurement. Moreover, gas flow is also a critical aspect that needs to be monitored in industrial and environmental applications.

Herein, utilizing the electric signal produced from the droplet/bubble *via* the capillary and the triboelectrification on the liquid/solid interface, a self-powered triboelectric microfluidic sensor (TMS) based on the TENG working in a single-electrode was successfully developed to detect both water and air flow. Through calculating the interval time between two signals and accumulating the signal number in a certain interval time, the flow rate and the flow volume can be obtained,

Received: July 5, 2016

Accepted: August 4, 2016

respectively. The detecting range and sensitivity of the sensor can be adjusted by employing capillary with different diameters. To study the properties of TMS, the voltage and current output mechanism of the sensor were illustrated, and the relationship between the droplet volume and the diameter of capillary was both experimentally measured and theoretically calculated. Finally, TMS was proposed to be a real-time monitor for both the patient's infusion process in actual medical situation and the gas flow of the industrial production. Results show that TMS has a big potential in building a self-powered micro total analysis system.

RESULTS AND DISCUSSION

The self-powered triboelectric microfluidic sensor (TMS) works on utilizing triboelectric nanogenerator working in a single electrode to detect the frequency and the number of droplet/bubble passing through the electrode. **Figure 1** a and b

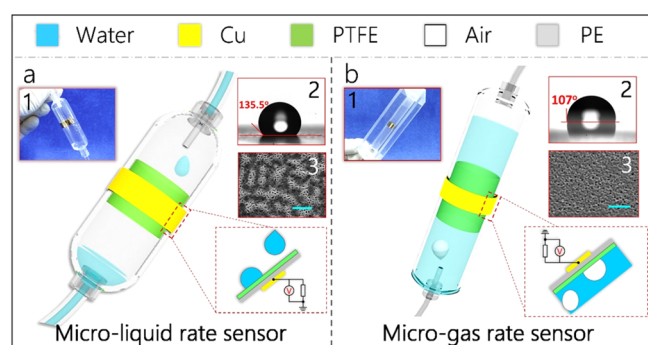


Figure 1. Structural schematic diagram of the sensor. (a) Structure of the liquid flow rate sensor, the inset 1 shows the photograph of the sensor fabricated on a medical infusion tube, the inset 2 shows the surface SEM image of PTFE layer (scale bar: 5 μm), the inset 3 shows the contact angle which indicates the hydrophobic property of the PTFE surface. (b) Structure of the gas flow rate sensor, the inset 1 shows the photograph of the sensor fabricated on a PE tube, the inset 2 shows the surface SEM image of PTFE layer (scale bar: 3 μm), the inset 3 shows the contact angle of the air bubble on the PTFE surface.

show the structural design of the microliquid flow sensor and microgas flow sensor, respectively. Typically, polyethylene (PE) tube is used as the substrate. Then, polytetrafluoroethylene (PTFE) is employed as the tribo-layer to modify the internal surface of the PE tube due to its hydrophobic and electret properties (charge can be retained for hundreds years).^{32,33,35,36} Finally, the copper layer is deposited on the outside surface of the PE tube as a single electrode of TENG. In the case of liquid flow sensor (**Figure 1a**), droplets are detached from the tip of capillary passing through TENG area so as to produce output signal. A zoomed-in view in **Figure 1a** shows the cross section schematic diagram of Liquid-TMS. A photograph of the Liquid-TMS fabricated on a infusion tube is depicted in the inset 1. It is important that the superhydrophobic surface of tribo-layer is needed to prevent water residual, which affects the output signal of TMS. Inset 2 and 3 illustrate the contact angle and the surface SEM image of the PTFE modified tribo-layer. In addition, in the case of gas flow sensor (**Figure 1b**), bubbles grow on the tip of capillary going through the TMS area so that voltage signal is induced. A zoomed-in view in **Figure 1b** is the cross section schematic diagram of Gas-TMS. And the photograph of the Gas-TMS is depicted in inset 1. It is

important that a suitable hydrophobic/hydrophilic surface of tribo-layer is necessary for the bubbles going through the tube and the output stability of Gas-TMS (**Supporting Information S1**). If the contact interface is completely hydrophilic, the generated tribo-charges will be screened by the adsorbed water between the tribo-layer and the air bubble, causing a small or none output signal. On the contrary, if the contact interface is superhydrophobic, the adsorption between gas and internal surface leads to the difficult transmission of air bubbles through the tube. Inset 2 and 3 show the contact angle and the surface SEM image of the PTFE modified tribo-layer. The detailed fabrication process is presented in the **Methods** section.

The output signal generation mechanism of TMS is based on the coupling of triboelectrification and electrostatic induction.^{15,37,38} In order to clearly illustrate the working mechanism, the charge distribution under short-circuit condition (schematic diagram) and the potential distribution under open-circuit condition (simulation) of both Liquid and Gas TMS in three states of a common cycle are displayed in **Figure 2**. It is known that, after interacting with water, PTFE surface could retain a layer of negative bound charges that do not dissipate in a long time.^{32,36} In the case of Liquid-TMS, before a droplet contacts the PTFE layer, the overlapped electrode is positively charged under short-circuit condition due to the electrostatic induction effect, and will establish a negative potential difference to the ground as shown in **Figure 2a I**. Later, when a water droplet falls down to contact the negatively charged PTFE layer, the negative charges on the PTFE will attract positive ions from the droplet to form an electric double layer (EDL) that must screen the electrostatic induction of negatively charged PTFE to the overlapped electrode, therefore, electrons will flow from the ground to the Cu electrode under short-circuit condition to reach a new electric equilibrium (**Figure 2a II**). Under open-circuit condition, due to the screen effect, there would be no potential difference between the Cu electrode and ground, as shown in **Figure 2a II**. Lastly, when the droplet leaves the PTFE layer, the screen effect will disappear and the overlapped electrode will be reinduced by positive charges under short-circuit condition and re-establish a negative potential difference between electrode and ground, as depicted in **Figure 2a III**. Once the following droplets are contacting the PTFE layer periodically, intermittent output signals will be obtained. In the case of Gas-TMS, the filled water forms a stable EDL on the water-PTFE interface to screen the electrostatic induction to the overlapped electrode until the air bubbles break down the screen effect. Typically, when an air bubble is rising to contact the PTFE layer, the formed EDL will be broken and the negative charge on the PTFE surface will induce the overlapped electrode to be positively charged, where the negative potential difference between the Cu electrode and ground drives electrons to flow from the electrode to the ground to reach an electric equilibrium. Later, when the air bubble leaves the PTFE layer, the EDL will be reformed, where the electrons flow from the ground to the electrode to neutralize the positive charges on the electrode. **Figure 2b I, II, III** illustrate the charge distribution and potential distribution of Gas-TMS in three states of a cycle.

On the basis of the above working mechanism, this TMS can monitor the number and frequency of the droplet/bubble. Besides, the capillary that produces regular droplet/bubble plays a critical role in TMS, and the effect parameters (such as the diameter, the material of the capillary, the liquid species, etc.) need to be systematically studied. In this part, steel

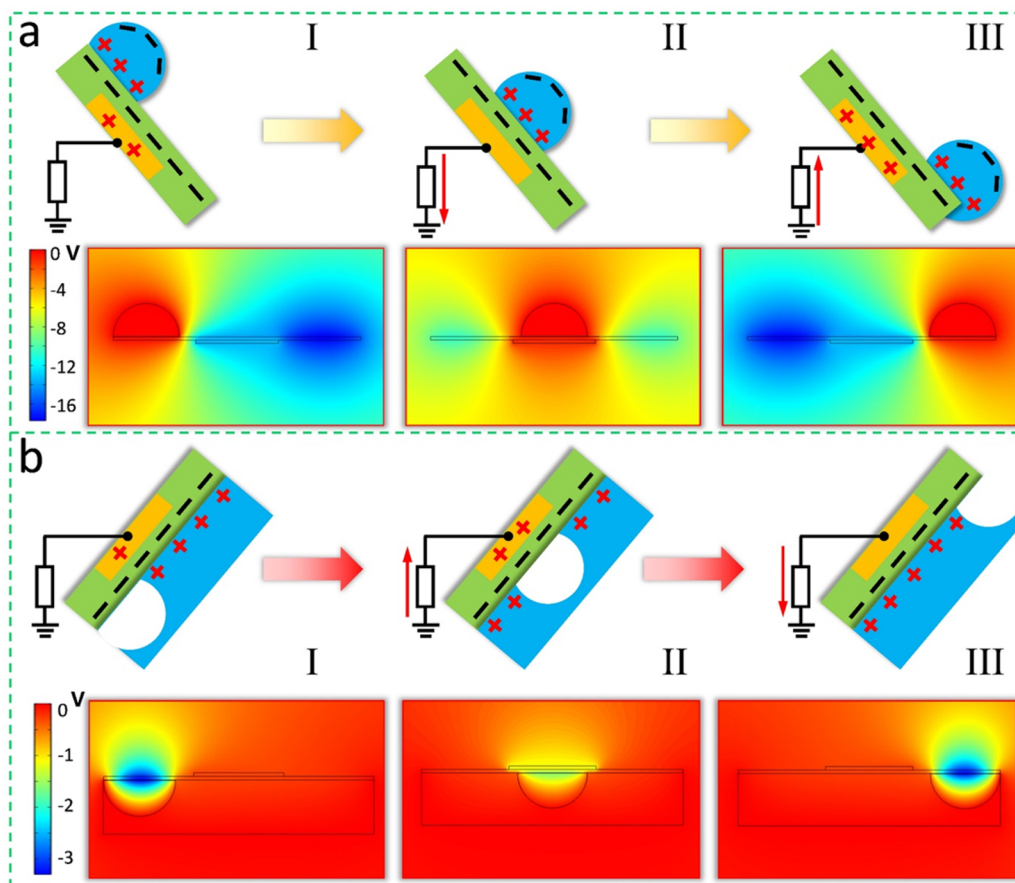


Figure 2. Working mechanism of the flow sensor. (a) Charge distribution schematic diagram (upper) under short circuit condition and the potential distribution (lower) under open circuit condition of the liquid flow sensor in a period cycle. (b) Charge distribution schematic diagram (upper) under short circuit condition and the potential distribution (lower) under open circuit condition of the gas flow sensor in a period cycle.

capillaries with different diameters (Supporting Information S2) are utilized to investigate the relationship between the volume of the droplet/bubble and the capillary diameter. In the case of water drop, Figure 3a presents three instantaneous pictures of water drops (the initial forming, before dropping, and just dropping state) formed on the tip of capillaries with 0.5, 0.8, and 1.0 mm diameters captured by high speed camera (Supporting Information S3), which reveals that the width of the droplet increases with the increase in the diameter of capillary. Moreover, by measuring the mass of hundreds droplets, the average volume of each water drop can be calculated as

$$V_{\text{drop}} = \frac{M}{\rho \cdot N} \quad (1)$$

where M , N , and ρ are the total mass of the hundreds droplets, the droplets number, and the density of the water, respectively.

The experimental results of V_{drop} for various capillaries are plotted in Figure 3b (symbols), it shows that the volume of each droplet increases almost linearly with the increase in the diameter of capillaries. Theoretically, Drop Volume/Weight mode³⁹ is chosen from various droplet forming modes (such as Wilhelmy Plate/Du Nouy Ring mode,^{40,41} Maximum Bubble Pressure mode,⁴² and Oscillating Jet mode⁴³) due to its easy operation and relatively accurate calculation. When the volume of the growing drop exceeds its maximum possible value, namely, the balance of forces acting vertically direction on the

droplet is broken, the droplet falls from the tip. Besides, the formation of such drops is strongly dependent on the surface or interfacial tension. According to Drop Volume mode, the part of the drop volume V_f falling from the capillary tip is given by

$$V_f(\rho_1 - \rho_g)g = 2\pi\sigma R\varphi \quad (2)$$

where ρ_1 and ρ_g are the densities of the water and air phases, respectively; g is the gravitational constant; σ is the surface tension of water ($\sigma = 7.28 \times 10^{-2}$ N/m); R is the radius of the capillary, and φ is the empirical drop correction factor introduced by Harkins and Brown.⁴⁴ Because the density of water is much greater than the air, the ρ_g can be negligible. Therefore, eq 2 can be expressed in dimensionless form

$$V_f = cR\varphi \quad (3)$$

where $c = 2\pi\sigma/\rho_1 g$. The value of the correction factor φ depends on $R/V_f^{1/3}$, so the correction factor φ is described by

$$\varphi = 1.007 - 1.479 \left(\frac{R}{V_f^{1/3}} \right) + 1.829 \left(\frac{R}{V_f^{1/3}} \right)^2$$

$$\frac{R}{V_f^{1/3}} < 0.3 \quad (4)$$

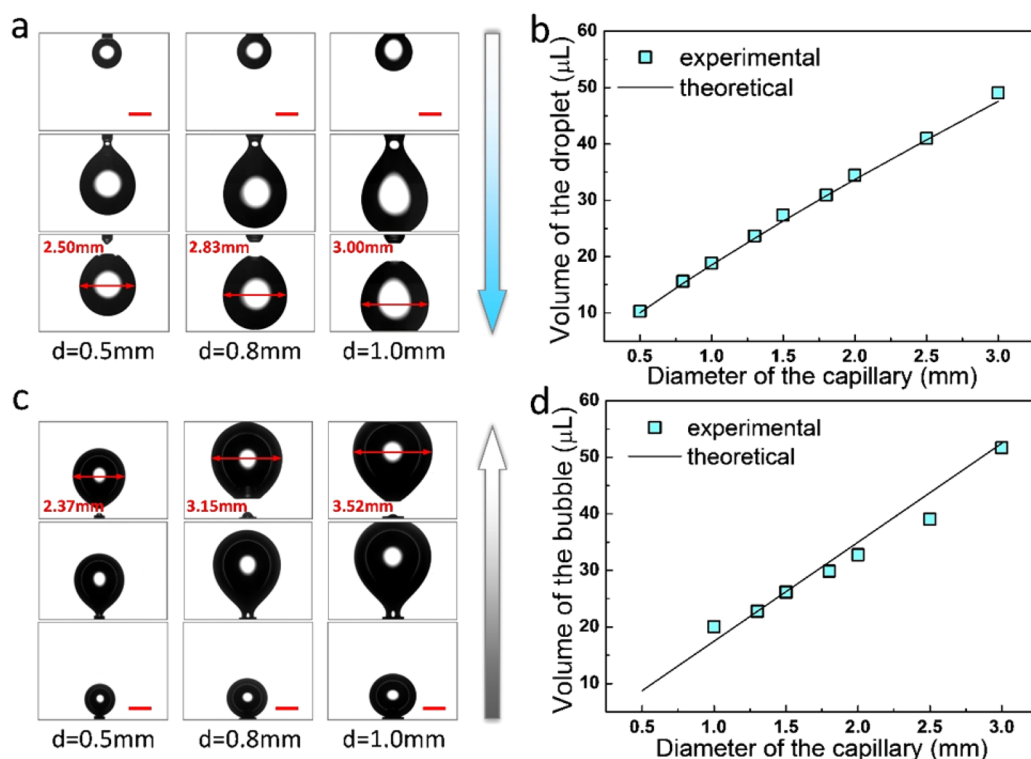


Figure 3. Relationship between the volume of the water droplet, air bubble and the diameter of the capillary. (a) Photographs show three states of the water droplets when using 0.5, 0.8, 1.0 mm capillaries. (b) Relationship between the volume of the liquid droplet and the diameter of the capillary both in experimental test and theoretical calculation. (c) Photographs show three states of the air bubble when using 0.5, 0.8, 1.0 mm capillaries. (d) Relationship between the volume of the air bubble and the diameter of the capillary both in experimental measurement and theoretical calculation.

$$\varphi = 0.9054 + 0.4293 \left(\frac{R}{V_f^{1/3}} \right)^2 - 0.7249 \left(\frac{R}{V_f^{1/3}} \right)$$

$$0.3 < \frac{R}{V_f^{1/3}} < 1.2 \quad (5)$$

According to eq 3–5, we have calculated the drop volume V_b as shown in Figure 3b (solid lines), and proved the proportional relationship between the volume of droplet and the diameter of capillary.

On the other hand, pictures of air bubbles formed at the tip of 0.5, 0.8, 1.0 mm capillaries, captured by high-speed camera (Supporting Information S4), are depicted in Figure 3c, which reveals that the width of the bubble has the same variation trend as that of the droplet (Figure 3a). In the same way, by measuring the time when hundreds bubbles are produced from microinjection pump, the average volume of each air bubble can be calculated as

$$V_{\text{bubble}} = \frac{vtd}{n} \quad (6)$$

where v , t , d , and n are the propel speed of the pump, the total time, the inner diameter of the injector, and the air bubble number, respectively.

The experimental measuring results of V_{bubble} for various capillaries are plotted in Figure 3d (symbols), which indicates that the volume of each air bubble linearly increases with the increase in diameter of capillaries. The size of the bubble is determined by the balance of forces applied on the bubble. The forces in the rise (vertical) direction acting on a bubble are

illustrated in Supporting Information S5. The gravity force (F_G) is

$$F_G = \rho_g V_B g \quad (7)$$

where the bubble density and volume are ρ_g and $V_B = \frac{4}{3}\pi r^3$ (the bubble is assumed to be spherical), respectively. The surface tension force (F_S) is⁴⁵

$$F_S = \frac{2\pi R^2 \sigma}{r} \quad (8)$$

where R and σ are the radius of capillary and surface tension of water. Finally, the buoyancy force (F_B) is⁴⁶

$$F_B = \rho_l V_B g \quad (9)$$

In the above force analysis, an important scale for the bubble volume is its radius r , by which gravity, buoyancy and surface tension are in balance. The bubble volume is described by

$$V_B = \frac{2\pi\sigma R}{(\rho_l - \rho_g)g} \quad (10)$$

with $\rho_l \gg \rho_g$, eq 10 becomes

$$V_B = \frac{2\pi\sigma R}{\rho_l g} \quad (11)$$

According to eq 11, we have calculated the bubble volume V_B , as shown in Figure 3d (solid lines), it proves the proportional relationship between the volume of bubble and the diameter of capillary. From the above discussion, it reveals that liquid and gas flow can be determined by monitoring the

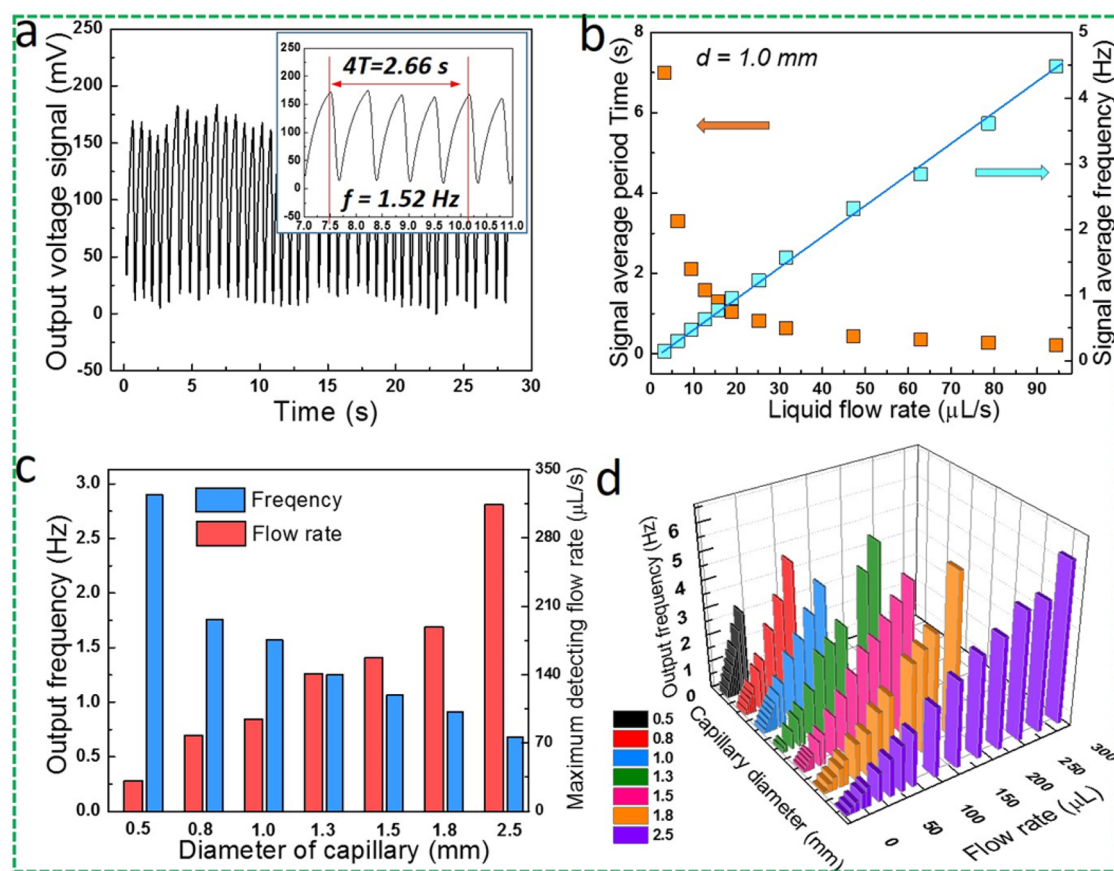


Figure 4. Electrical measurement of the Liquid-TMS. (a) Output voltage signal of liquid flow rate sensor, and the inset shows frequency of signals. (b) Dependence of the signal average period time/frequency on liquid flow rate measured at 1.0 mm capillary. (c) Output of frequency of TMS with different capillaries under a certain flow ($\sim 30 \mu\text{L/s}$) and maximum detecting range of TMS with different capillaries. (d) 3D graph shows the output frequency of TMS with various capillaries under different external flow rate.

droplets and bubbles. Moreover, by employing different capillaries, the characteristics of TMS can be adjusted.

To measure the electrical output performance of the TMS, a microinjection pump is employed to provide a continuously stable fluidic flow. In the case of Liquid-TMS, the output voltage signal of TMS (capillary diameter, 1.5 mm; flow rate, $\sim 47 \mu\text{L/s}$) is presented in Figure 4a (the current signal is shown in Supporting Information S6a). It is worth to note that, the hydrophilic tribo-layer will affect the output signal of the sensor due to the residual water (the output voltage signal is shown in Supporting Information S7). In addition, the ion concentration of the solution will also affect the output of the sensor as shown in Supporting Information S8. From the voltage signal, the output frequency (1.52 Hz) can be calculated by the interval time between two signal peaks. In the following discussion, signal frequency (f_s) is used as the sensing factor. In order to systematically demonstrate the performance of TMS, the f_s value of Liquid-TMS with 1.0 mm capillary under different external water flow (from $\sim 3 \mu\text{L/s}$ to $\sim 95 \mu\text{L/s}$) is measured (the voltage output curve is represented in Supporting Information S9) and plotted in Figure 4b, showing the proportional relationship between f_s and flow rate for a certain Liquid-TMS, and proving that the device is highly suitable to be used as a flow rate sensor (The other measurement of Liquid-TMS with different sizes of capillary is shown in Supporting Information S10). In addition, by accumulating the signal peak numbers, the flux can be obtained, too. It is worth noting that Liquid-TMS with a smaller capillary

has a larger output frequency under a certain external water flow (namely a higher sensitivity). However, TMS with a larger capillary can get a wider detecting range, because a smaller capillary is easier to form nondistinguishable water droplets with the increase in flow rate, which cannot be detected by TMS. Actually, the detecting range may be affected by the tilt angle of the sensor. Therefore, the theoretical analysis and experimental measurement were conducted to explore the relationship between the detecting range and tilt angle, shown in Supporting Information S11 and 12. Figure 4c represents the output frequency under external water flow rate of $\sim 30 \mu\text{L/s}$ and the maximum detecting flow rate of TMS with various capillaries (0.5, 0.8, 1.0, 1.3, 1.5, 1.8, 2.5 mm). The results prove that the sensitivity and detecting range can be adjusted by choosing different capillaries. 3D graph in Figure 4d depicts a comprehensive characteristic of each Liquid-TMS.

In the case of Gas-TMS, the measured voltage signal (capillary: 1.0 mm, flow rate: $\sim 30 \mu\text{L/s}$) is depicted in Figure 5a (the current signal is shown in Supporting Information S6b), from which the signal frequency (f_s) can be calculated. Here, both the voltage and current output of Gas-TMS are several-folds smaller than that of Liquid-TMS, because Liquid-TMS works in the continuously friction between water droplet and PTFE layer and a relatively larger contact area. In order to systematically illustrate the performance of Gas-TMS, the f_s value of a TMS with 3.0 mm capillary under different external air flow (from $\sim 7 \mu\text{L/s}$ to $\sim 280 \mu\text{L/s}$) is measured (the voltage output curve is represented in Supporting Information S13)

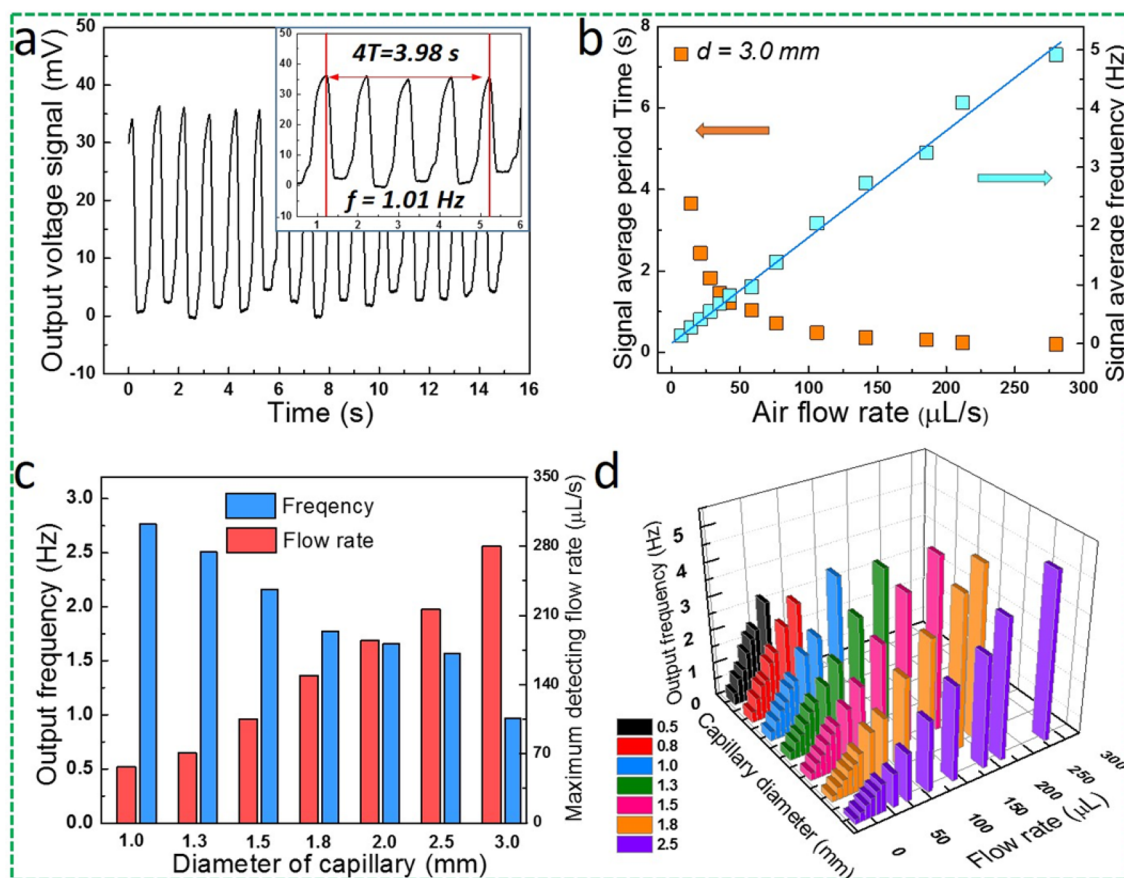


Figure 5. Electrical measurement of the Gas-TMS. (a) Output voltage signal of gas flow rate sensor, and the inset shows frequency of signals. (b) Dependence of the signal average period time/frequency on gas flow rate measured at 3.0 mm capillary. (c) Output of frequency of TMS with different capillaries under a certain flow ($\sim 60 \mu\text{L/s}$) and maximum detecting range of TMS with different capillaries. (d) 3D graph shows the output frequency of TMS with various capillaries under different external flow rate.

and plotted in Figure 5b, indicating the proportional relationship between f_s and flow rate for a certain Gas-TMS (the other measurement of Gas-TMS is shown in Supporting Information S14). Figure 5c shows the output frequency (under external air flow rate of $\sim 60 \mu\text{L/s}$) and the maximum detecting flow rate of TMS with various capillaries (1.0, 1.3, 1.5, 1.8, 2.0, 2.5, 3.0 mm). It reveals that the sensitivity and detecting range of Gas-TMS can also be adjusted by choosing different capillaries. 3D graph in Figure 5d represents a comprehensive characteristic of each Gas-TMS.

The designed Liquid/Gas-TMS could be applied in medical and industrial field to realize the self-powered system, such as monitoring infusion, detecting gas flow. To demonstrate this, first, the Liquid-TMS is vertically fixed in an infusion tube with a tilting angle of 60° away from the horizontal position. When the patient is treated by infusion, namely, liquid medicine passing through TMS area, pulse of voltage is produced and collected. At the same time, the collected data is transferred to a computer to realize real-time display by the data capture device (Figure 6a). A zoomed-in view in Figure 6a is the photography of the infusion tube. Pulses of voltage are produced, as shown in Figure 6b. When the infusion speed varies from 3.14 to $62.8 \mu\text{L/s}$, different output frequencies of signals are obtained (from 0.2 to 3.0 Hz), from which we can calculate the interval of each droplet. On the other hand, the flux of medicine liquid can be calculated in a certain time by counting the number of output peaks. This demonstration clearly indicates that the device can

be potentially used in infusion set to give an accurate monitoring. Besides, the device can also be possibly used as a detector to drive an alarm work if there is no output signal due to lack of medicine liquid or backflow of blood. Therefore, precise control to the infusion flow can be achieved through this simple and feasible method.

Second, the Gas-TMS can be used to detect gas flow in industrial applications. The device is vertically fixed on an acrylic frame with a tilting angle of 30° away from the horizontal position. When the injector is driven by the pump, the well-formed air bubbles attach to or detach from the surface of PTFE in the tube and then produce the pulse of voltage. At the same time, the collected data is transferred to a computer to realize real-time display by the data capture device (Figure 6c). A zoomed-in view in Figure 6c is the photography of device. Pulses of voltage are produced, as shown in Figure 6d. When the production speed of bubbles varies from 7.06 to $58.9 \mu\text{L/s}$, different frequencies of output signals are obtained (from 0.2 to 1.65 Hz). According to the number of peaks of output signals, the flux in a certain time and velocity of air bubbles can be obtained. Therefore, we believe that this device has great potential in the detection of air flow. This concept will not only be limited to the air detection system, but also has the potential to be applied in other gas detection system.

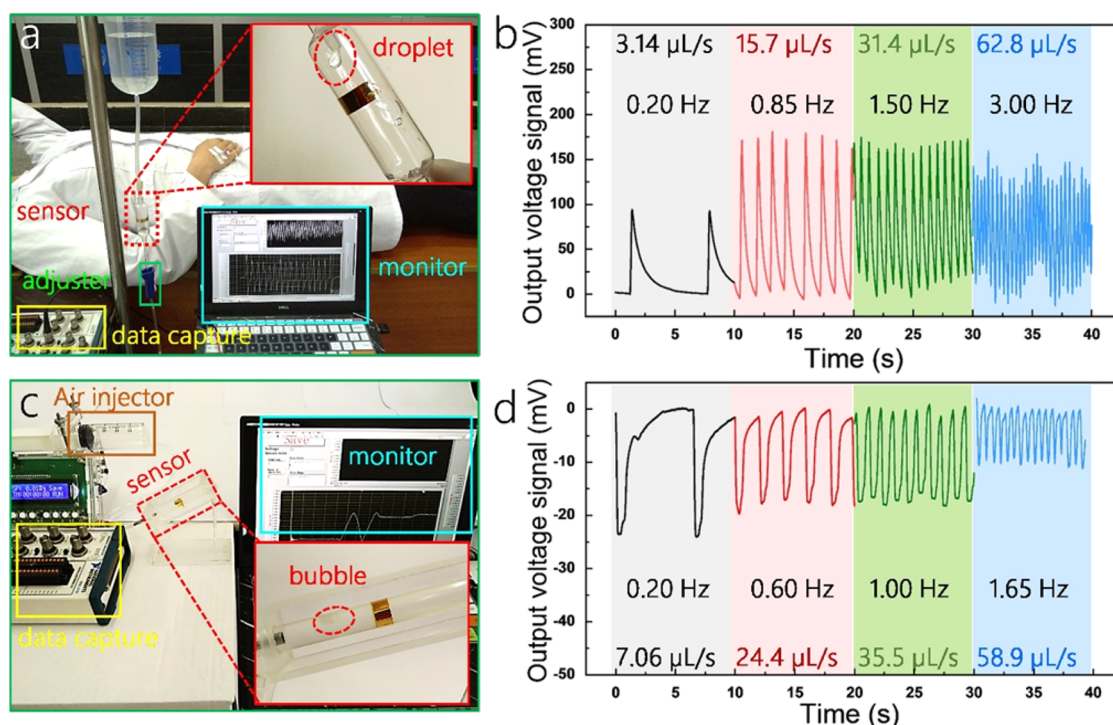


Figure 6. Application in self-powered system. (a) Infusion monitor using the liquid flow sensor. (b) Output voltage of the infusion monitor measured at flow rate from 3.14 to 62.8 $\mu\text{L/s}$. (c) Gas detector with the gas flow sensor. (d) Output voltage of the gas detector measured at air rate from 7.06 to 58.9 $\mu\text{L/s}$.

CONCLUSION

In summary, a facile triboelectric self-powered microfluidic sensor has been developed for liquid flow and gas flow detection. The detecting mechanism and the output principle for both liquid flow and gas flow TMS are systematically illustrated and is discussed. Through calculating the interval between two signals and accumulating the signals in a certain interval, the flow rate and the flux can be obtained, respectively. The volume of per droplet/bubble produced by different diameter capillaries is experimentally and theoretically studied. Measurement and analysis of the output signals of TMS using different capillaries indicate that the output frequency has a linear relationship with flow rate. The TMS utilizing smaller capillary can get a relatively higher sensitivity, whereas the TMS using larger capillary can get a wider detecting range. In addition, the TMS can be used as a real-time monitor for patient's infusion process in hospitals and the gas-flow of the industrial production. Results show that TMS has a big potential in building a self-powered micro total analysis system for commercial applications.

METHODS

Fabrication of the Microfluidic Sensor. First, PE tube (diameter: 9 mm, thickness: 0.1 mm) was used as the substrate for both liquid (4 cm in length) and gas (8 cm in length) flow sensor fabrication. In order to prepare a hydrophobic trilayer, PTFE aqueous suspension (Dupont, 60 wt %, aqueous) was dropped through the internal surface of the PE tube, and then cured in a vacuum oven at 80 °C for 5 h (3 cycles for the liquid sensor and 1 cycle for the gas sensor). It is worth noting that a superhydrophobic property and a suitable hydrophobic/hydrophilic property play a critical role in the liquid and gas flow sensor, respectively. Second, a 4 mm width ring-like

copper electrode was deposited on the outside surface of the PE tube (Liquid-TMS: 1 cm away from the front part. Gas-TMS: 4 cm away from the front part) using physical vapor deposition (PVD 75). And then, the copper wire was connected to the copper layer for electric measurement. Finally, an acrylic frame was used to fix the sensor with a certain tilt angle, and steel capillaries (diameter from 0.5 mm to 3.0 mm) with a certain height (1.5 cm) were employed to produce water (tap water) droplets and air bubbles (PE tube filled with tap water) with different diameters.

Experimental Setup for Quantitative Measurement. A JEOL JSM-7800F field emission scanning electron microscope (SEM) was used to measure the morphology of PTFE on PE substrate. Both the contact angle and the formation process of the droplet/bubble were characterized by a high-speed camera (Phantom V7.3). Microinjection pump was used to supply a stable liquid/gas flow. A programmable electrometer (Keithley 6514) was adopted to test the output voltage signal of the sensor. The software platform is constructed based on LabView, which is capable of realizing real-time data acquisition control and analysis. COMSOL MULTIPHYSICS software was employed for potential distribution simulation.

ASSOCIATED CONTENT

Supporting Information

These materials are available free of charge *via* the Internet at The Supporting Information is available free of charge on the ACS Publications website at DOI: 10.1021/acsnano.6b04440.

(Supporting Information S1) The scheme of hydrophilic and superhydrophobic surface for air bubble. (Supporting Information S2) The digital photography of steel capillaries from 0.5 to 3 mm diameter. (Supporting Information S3) Sketch of apparatus for measuring the

water droplets. (Supporting Information S4) Schematic diagram of the experimental facility for measuring the air bubbles. (Supporting Information S5) Schematic diagram of the vertical forces on a bubble during formation from a capillary tip. (Supporting Information S6) The output current signal of the sensor. (Supporting Information S7) The output voltage signal of the Liquid-TMS when using Kapton as tribo-layer. (Supporting Information S8) The output amplitude of the Liquid-TMS when using different concentration of NaCl aqueous solution. (Supporting Information S9) The output voltage curve of Liquid-TMS under various external flow rate. (Supporting Information S10) Dependence of the signal average period time/frequency on liquid flow rate measured at 0.5, 0.8, 1.0, 1.3, 1.5, 1.8, 2.5 mm capillaries. (Supporting Information S11) Schematic diagram of the forces on a droplet during the movement process in the inner wall of PE tube. (Supporting Information S12) The photography of the droplet formed by 1 mm capillary passing through the electrode at different tilt angle (15°, 33°, 47°, 66°). (Supporting Information S13) The output voltage curve of Gas-TMS under various external flow rate. (Supporting Information S14) Dependence of the signal average period time/frequency on gas flow rate measured at 1.0, 1.3, 1.5, 1.8, 2.0, 2.5, 3.0 mm capillaries. (PDF)

AUTHOR INFORMATION

Corresponding Authors

*E-mail: hucg@cqu.edu.cn.

*E-mail: zhong.wang@mse.gatech.edu.

Author Contributions

§(J.C. and H.G.) These authors contributed equally to this work.

Notes

The authors declare no competing financial interest.

ACKNOWLEDGMENTS

This work is supported by NSFC (51572040), the Fundamental Research Funds for the Central Universities (CQDXWL-2014-001), and the National High Technology Research and Development Program (863 program) of China (2015AA034801)

REFERENCES

- (1) Manz, A.; Graber, N.; Widmer, H. M. Miniaturized Total Chemical Analysis Systems: A Novel Concept for Chemical Sensing. *Sens. Actuators, B* **1990**, *1*, 244–248.
- (2) Whitesides, G. M. The Origins and the Future of Microfluidics. *Nature* **2006**, *442*, 368–373.
- (3) Campopiano, S.; Bernini, R.; Zeni, L.; Sarro, P. M. Microfluidic Sensor Based on Integrated Optical Hollow Waveguides. *Opt. Lett.* **2004**, *29*, 1894–1896.
- (4) Johnson, R. G.; Higashi, R. E. A Highly Sensitive Silicon Chip Microtransducer for Air Flow and Differential Pressure Sensing Applications. *Sens. Actuators* **1987**, *11*, 63–72.
- (5) Ohnstein, T. R.; Johnson, R. G.; Higashi, R. E.; Burns, D. W. In *Environmentally Rugged, Wide Dynamic Range Microstructure Airflow Sensor, 4th Technical Digest*; Institute of Electrical and Electronics Engineers (IEEE): Piscataway, NJ, 1990; pp 158–160.
- (6) Shaban, H.; Tavoularis, S. The Wire-Mesh Sensor As a Two-Phase Flow Meter. *Meas. Sci. Technol.* **2015**, *26*, 015306.

- (7) Swart, N. R.; Nathan, A. Flow-Rate Microsensor Modelling and Optimization Using SPICE. *Sens. Actuators, A* **1992**, *34*, 109–122.
- (8) Kinoshita, H.; Kaneda, S.; Fujii, T.; Oshima, M. Three-Dimensional Measurement and Visualization of Internal Flow of a Moving Droplet Using Confocal Micro-PIV. *Lab Chip* **2007**, *7*, 338–346.
- (9) Qiu, L.; Hein, S.; Obermeier, E.; Schubert, A. Micro Gas-Flow Sensor with Integrated Heat Sink and Flow Guide. *Sens. Actuators, A* **1996**, *54*, 547–551.
- (10) Lindken, R.; Rossi, M.; Grosse, S.; Westerweel, J. Micro-Particle Image Velocimetry (MicroPIV): Recent Developments, Applications, and Guidelines. *Lab Chip* **2009**, *9*, 2551–2567.
- (11) Rahman, M. F. A.; Nawi, M. N. M.; Manaf, A. A.; Arshad, M. R. Characterization of Microfluidic-Based Acoustic Sensor for Immersion Application. *IEEE Sens. J.* **2015**, *15*, 1559–1566.
- (12) Koppaathy, V. L.; Tangutooru, S. M.; Nestorova, G. G.; Guilbeau, E. J. Thermoelectric Microfluidic Sensor for Bio-Chemical Applications. *Sens. Actuators, B* **2012**, *166–167*, 608–615.
- (13) Zougagh, M.; Rios, A. Micro-Electromechanical Sensors in the Analytical Field. *Analyst* **2009**, *134*, 1274–1290.
- (14) Waggoner, P. S.; Craighead, H. G. Micro and Nanomechanical Sensors for Environmental, Chemical, and Biological Detection. *Lab Chip* **2007**, *7*, 1238.
- (15) Fan, F. R.; Tian, Z. Q.; Wang, Z. L. Flexible Triboelectric Generator. *Nano Energy* **2012**, *1*, 328–334.
- (16) Fan, F. R.; Lin, L.; Zhu, G.; Wu, W.; Zhang, R.; Wang, Z. L. Transparent Triboelectric Nanogenerators and Self-Powered Pressure Sensors Based on Micropatterned Plastic Films. *Nano Lett.* **2012**, *12*, 3109–3114.
- (17) Yang, Y.; Zhu, G.; Zhang, H.; Chen, J.; Zhong, X.; Lin, Z. H.; Su, Y.; Bai, P.; Wen, X.; Wang, Z. L. Triboelectric Nanogenerator for Harvesting Wind Energy and As Self-Powered Wind Vector Sensor System. *ACS Nano* **2013**, *7*, 9461–9468.
- (18) Zi, Y.; Niu, S.; Wang, J.; Wen, Z.; Tang, W.; Wang, Z. L. Standards and Figure-of-Merits for Quantifying the Performance of Triboelectric Nanogenerators. *Nat. Commun.* **2015**, *6*, 8376.
- (19) Guo, H.; Leng, Q.; He, X.; Wang, M.; Chen, J.; Hu, C.; Xi, Y. A Triboelectric Generator Based on Checker-Like Interdigital Electrodes with a Sandwiched PET Thin Film for Harvesting Sliding Energy in All Directions. *Adv. Energy Mater.* **2015**, *5*, 1400790.
- (20) Zheng, Y.; Cheng, L.; Yuan, M.; Wang, Z.; Zhang, L.; Qin, Y.; Jing, T. An Electrospun Nanowire-Based Triboelectric Nanogenerator and Its Application in a Fully Self-Powered UV Detector. *Nanoscale* **2014**, *6*, 7842–7846.
- (21) Wang, S.; Lin, L.; Wang, Z. L. Triboelectric Nanogenerators as Self-Powered Active Sensors. *Nano Energy* **2015**, *11*, 436–462.
- (22) Zhong, J.; Zhang, Y.; Zhong, Q.; Hu, Q.; Hu, B.; Wang, Z. L.; Zhou, J. Fiber-Based Generator for Wearable Electronics and Mobile Medication. *ACS Nano* **2014**, *8*, 6273–6280.
- (23) Zhong, J.; Zhu, H.; Zhong, Q.; Dai, J.; Li, W.; Jang, S. H.; Yao, Y.; Henderson, D.; Hu, Q.; Hu, L.; Zhou, J. Self-Powered Human-Interactive Transparent Nanopaper Systems. *ACS Nano* **2015**, *9*, 7399–7406.
- (24) Zhong, J.; Zhong, Q.; Hu, Q.; Wu, N.; Li, W.; Wang, B.; Hu, B.; Zhou, J. Stretchable Self-Powered Fiber-Based Strain Sensor. *Adv. Funct. Mater.* **2015**, *25*, 1798–1803.
- (25) Chen, J.; Zhu, G.; Yang, W.; Jing, Q.; Bai, P.; Yang, Y.; Hou, T. C.; Wang, Z. L. Harmonic-Resonator-Based Triboelectric Nanogenerator As a Sustainable Power Source and a Self-Powered Active Vibration Sensor. *Adv. Mater.* **2013**, *25*, 6094–6099.
- (26) Zhang, H.; Yang, Y.; Su, Y.; Chen, J.; Adams, K.; Lee, S.; Hu, C.; Wang, Z. L. Triboelectric Nanogenerator for Harvesting Vibration Energy in Full Space and As Self-Powered Acceleration Sensor. *Adv. Funct. Mater.* **2014**, *24*, 1401–1407.
- (27) Guo, H.; Chen, J.; Tian, L.; Leng, Q.; Xi, Y.; Hu, C. Airflow-Induced Triboelectric Nanogenerator As a Self-Powered Sensor for Detecting Humidity and Airflow Rate. *ACS Appl. Mater. Interfaces* **2014**, *6*, 17184–17189.

- (28) Yang, W.; Chen, J.; Wen, X.; Jing, Q.; Yang, J.; Su, Y.; Zhu, G.; Wu, W.; Wang, Z. L. Triboelectrification Based Motion Sensor for Human-Machine Interfacing. *ACS Appl. Mater. Interfaces* **2014**, *6*, 7479–7484.
- (29) Yi, F.; Lin, L.; Niu, S.; Yang, J.; Wu, W.; Wang, S.; Liao, Q.; Zhang, Y.; Wang, Z. L. Self-Powered Trajectory, Velocity, and Acceleration Tracking of a Moving Object/Body Using a Triboelectric Sensor. *Adv. Funct. Mater.* **2014**, *24*, 7488–7494.
- (30) Yang, J.; Chen, J.; Su, Y.; Jing, Q.; Li, Z.; Yi, F.; Wen, X.; Wang, Z.; Wang, Z. L. Eardrum-Inspired Active Sensors for Self-Powered Cardiovascular System Characterization and Throat-Attached Anti-Interference Voice Recognition. *Adv. Mater.* **2015**, *27*, 1316–1326.
- (31) Jung, W. S.; Kang, M. G.; Moon, H. G.; Baek, S. H.; Yoon, S. J.; Wang, Z. L.; Kim, S.-W.; Kang, C. Y. High Output Piezo/Triboelectric Hybrid Generator. *Sci. Rep.* **2015**, *5*, 9309.
- (32) Zhu, G.; Su, Y.; Bai, P.; Chen, J.; Jing, Q.; Yang, W.; Wang, Z. L. Harvesting Water Wave Energy by Asymmetric Screening of Electrostatic Charges on a Nanostructured Hydrophobic Thin-Film Surface. *ACS Nano* **2014**, *8*, 6031–6037.
- (33) Lin, Z. H.; Cheng, G.; Lee, S.; Pradel, K. C.; Wang, Z. L. Harvesting Water Drop Energy by a Sequential Contact-Electrification and Electrostatic-Induction Process. *Adv. Mater.* **2014**, *26*, 4690–4696.
- (34) Li, X.; Yeh, M. H.; Lin, Z. H.; Guo, H.; Yang, P. K.; Wang, J.; Wang, S.; Yu, R.; Zhang, T.; Wang, Z. L. Self-Powered Triboelectric Nanosensor for Microfluidics and Cavity-Confined Solution Chemistry. *ACS Nano* **2015**, *9*, 11056–11063.
- (35) Zhong, J.; Zhong, Q.; Fan, F.; Zhang, Y.; Wang, S.; Hu, B.; Wang, Z. L.; Zhou, J. Finger Typing Driven Triboelectric Nanogenerator and Its Use for Instantaneously Lighting up LEDs. *Nano Energy* **2013**, *2*, 491–497.
- (36) Malecki, J. A. Linear Decay of Charge in Electrets. *Phys. Rev. B: Condens. Matter Mater. Phys.* **1999**, *59*, 9954–9960.
- (37) Guo, H.; He, X.; Zhong, J.; Zhong, Q.; Leng, Q.; Hu, C.; Chen, J.; Tian, L.; Xi, Y.; Zhou, J. A Nanogenerator for Harvesting Airflow Energy and Light Energy. *J. Mater. Chem. A* **2014**, *2*, 2079–2087.
- (38) Guo, H.; Chen, J.; Yeh, M. H.; Fan, X.; Wen, Z.; Li, Z.; Hu, C.; Wang, Z. L. An Ultrarobust High-Performance Triboelectric Nanogenerator Based on Charge Replenishment. *ACS Nano* **2015**, *9*, 5577–5584.
- (39) Vazquez, A.; Leifer, I.; Sánchez, R. M. Consideration of the Dynamic Forces During Bubble Growth in a Capillary Tube. *Chem. Eng. Sci.* **2010**, *65*, 4046–4054.
- (40) Wu, N.; Dai, J.; Micale, F. J. Dynamic Surface Tension Measurement with a Dynamic Wilhelmy Plate Technique. *J. Colloid Interface Sci.* **1999**, *215*, 258–269.
- (41) Lee, B. B.; Chan, E. S.; Ravindra, P.; Khan, T. A. Surface Tension of Viscous Biopolymer Solutions Measured Using the Du Nouy Ring Method and The Drop Weight Methods. *Polym. Bull.* **2012**, *69*, 471–489.
- (42) Hollowell, C. P.; Hirt, D. E. Unusual Characteristics of the Maximum Bubble Pressure Method Using a Teflon Capillary. *J. Colloid Interface Sci.* **1994**, *168*, 281–288.
- (43) Oberleithner, K.; Rukes, L.; Soria, J. Mean Flow Stability Analysis of Oscillating Jet Experiments. *J. Fluid Mech.* **2014**, *757*, 1–32.
- (44) Wilkinson, M. C.; Kidwell, R. L. A Mathematical Description of the Harkins And Brown Correction Curve for the Determination of Surface and Interfacial Tensions. *J. Colloid Interface Sci.* **1971**, *35*, 114–119.
- (45) Duhar, G.; Colin, C. Dynamics of Bubble Growth and Detachment in a Viscous Shear Flow. *Phys. Fluids* **2006**, *18*, 077101.
- (46) Terasaka, K.; Tsuge, H. Bubble Formation under Constant-Flow Conditions. *Chem. Eng. Sci.* **1993**, *48*, 3417–3422.